

Digital Modeling of Spatial Pathway Activity from Histology Reveals Tumor Microenvironment Heterogeneity

Ling Liao^{1,2,3,*}, Changhui Yang⁴, Maxim Artyomov¹, Mark Watson¹, Adam Kepecs⁵, Haowen Zhou⁴, Alexey Sergushichev,¹ Richard Cote^{1,*}

1, Department of Pathology and Immunology, School of Medicine, Washington University, St Louis, MO, USA, 63108.

2. Computational and systems biology, Division of Biology & Biomedical Sciences, Washington University in St Louis, MO, USA, 63108.

3. Biomedical Deep Learning LLC, St Louis, MO, USA, 63130.

4. Department of Electrical Engineering, California Institute of Technology, Pasadena, California USA, 91125.

5. Department of Neuroscience, School of Medicine, Washington University, St. Louis, MO, USA, 63108.

* Correspondence:

Richard Cote, rcote@wustl.edu,

Ling Liao, 1995aileen@gmail.com

Abstract

Spatial transcriptomics (ST) enables simultaneous mapping of tissue morphology and spatially resolved gene expression, offering unique opportunities to study tumor microenvironment heterogeneity. Here, we introduce a computational framework that predicts spatial pathway activity directly from hematoxylin-and-eosin-stained histology images at microscale resolution (55–100 μm). Using image features derived from a computational pathology foundation model, we found that TGF β signaling was the most accurately predicted pathway across three independent breast and lung cancer ST datasets. In 87–88% of reliably predicted cases, the resulting spatial TGF β activity maps reflected the expected contrast between tumor and adjacent non-tumor regions, consistent with the known role of TGF β in regulating interactions within the tumor microenvironment. Notably, linear and nonlinear predictive models performed similarly, suggesting that image features may relate to pathway activity in a predominantly linear fashion or that nonlinear structure is small relative to measurement noise. These findings demonstrate that features extracted from routine histopathology may recover spatially coherent and biologically interpretable pathway patterns, offering a scalable strategy for integrating image-based inference with ST information in tumor microenvironment studies.

Introduction

Spatial transcriptomics (ST) offers a powerful approach to study the spatial organization and heterogeneity of gene expression within tissue sections.^[1,2,3] However, the broad application of ST is limited by its high expense—each section often costs several thousand dollars—making it unsuitable for experiments involving many samples, such as longitudinal assessments of tissues from multiple experimental animals and patients.^[3,4,5,6] To address this barrier, several deep learning-based methods have been developed to predict spatial gene expression from paired histology images, potentially extending the utility of widely available and cost-effective hematoxylin-and-eosin (H&E) slides. Wang et al. (2025) systematically evaluated eleven such methods, demonstrating that they exhibit some predictive potential for single-gene spatial

expression, with overall Pearson correlation coefficient around 0.1 at spot resolution (see Wang et al., Fig. 2d).^[7] They further assessed clinical relevance by using predicted pseudobulk gene expression for survival analysis in TCGA-BRCA patients at the whole-slide level rather than individual spot resolution.^[7]

While encouraging, the expression of individual genes is inherently stochastic.^[8,9,10] Low-abundance or highly variable genes—often biologically informative—remain difficult to quantify accurately, even with experimental ST data. Moreover, histology-derived features are intrinsically limited in capturing certain regulatory or signaling pathways, and can only capture a small fraction of the underlying transcriptional variability. Additional noise or inconsistencies introduced by protocol- or patient-specific batch effects further compromises the reliability and reproducibility of both measured and image-derived expression values across datasets.^[7] Furthermore, Pearson's *r* mainly measures numerical similarity rather than the fidelity of spatial expression patterns; therefore, a low Pearson's *r* does not inherently imply poor spatial prediction performance.^[11]

These limitations suggest that shifting from single-gene to pathway-level modeling might provide a more robust and interpretable strategy. We hypothesize that histology-derived features might robustly encode morphological cues that reflect coordinated, pathway-level transcriptional programs at spot resolution. We further hypothesize that the pathway most accurately predicted may correspond to well-known morphological distinctions across micro tissue regions, such as tumor versus adjacent non-tumor areas. If certain pathway—such as TGF β signaling—can be reliably predicted from paired histology-derived features, analyzing the predicted spatial expression differences across tumor and tumor microenvironment regions might (i) reveal signaling networks underlying the tumor ecosystem^[12,13], (ii) inform targeted and combination immunotherapies^[14,15], and (iii) ultimately support the use of histology features to reliably predict treatment response, reducing false positives and false negatives.

Building on these premises, we developed a computational framework to predict the enrichment of seven well-characterized signaling pathways relevant to tumor biology and cellular regulation. Predictions were generated from histology-based features at approximately 100- and 55- μ m resolutions. Applied to independent breast and lung cancer ST datasets, the framework predicted TGF β signaling most accurately comparing with other pathways, consistent with its known role in modulating tumor–microenvironment interactions. Furthermore, the pipeline successfully distinguished tumor microregions from adjacent non-tumor micro areas, demonstrating that the histology-derived features capture biologically meaningful differences between histologically distinct regions. These results highlight the potential of integrating histology and inferred pathway-level transcriptomics to map tumor microenvironment signaling landscapes, offering a scalable and interpretable approach for spatial pathway analysis and potentially guiding therapeutic strategies.

Results

Study design

We hypothesize that histology-derived features may robustly capture morphological cues and reflect coordinated, pathway-level transcriptional programs at spot resolution. To test this (Fig. 1a), we first extracted 1,536 features from 112×112 pixel H&E image spots at approximately

55–100 μm resolutions. Feature extraction was performed using the UNI2 pathology foundation model, and its embeddings (UNI2-h) were pretrained on over 200 million H&E and immunohistochemistry images from more than 350,000 diverse whole-slide images sourced from Mass General Brigham^[16], none of which overlapped with the histology data used in our study.

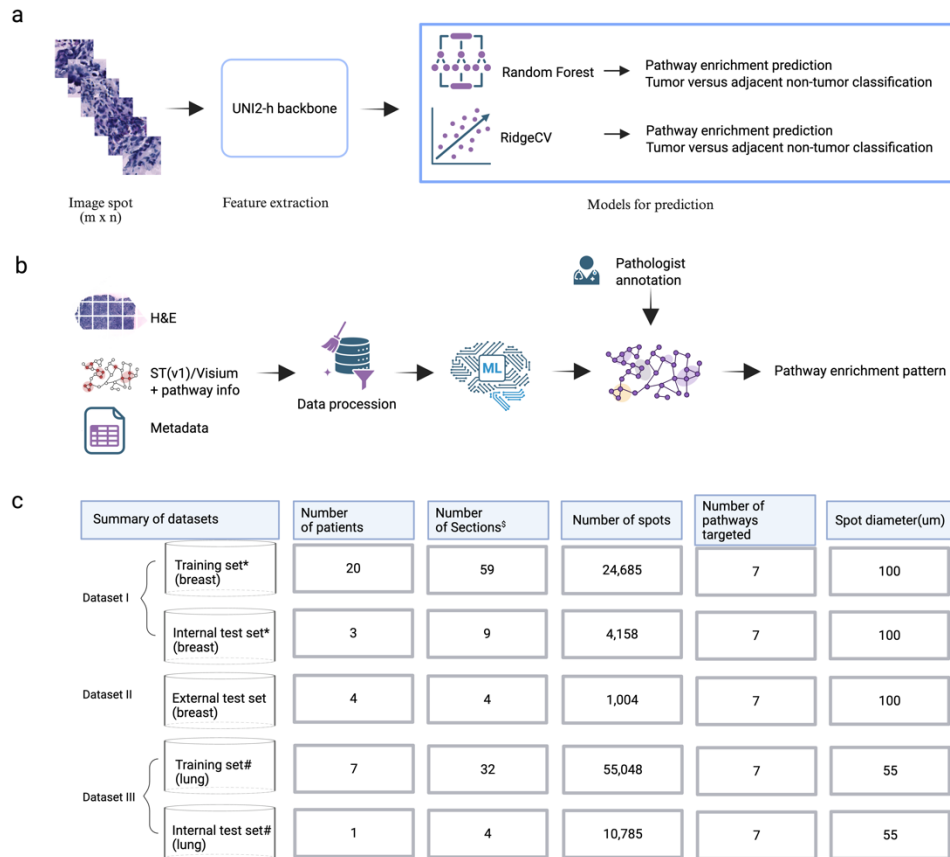
Reference pathway enrichment activities were computed using PROGENy^[17], a computational tool that captures pathway enrichment by integrating the expression of downstream target genes, thereby accounting for post-translational effects that may be reflected in morphology-derived features.

The extracted visual features were used as input to Random Forest (RF) models to predict pathway enrichment scores as well as tumor and adjacent non-tumor microregions at the corresponding resolutions. The prediction of tumor versus adjacent non-tumor microregions served to validate that histology-derived features adequately capture information distinguishing tumors from surrounding micro regions.

To evaluate our second hypothesis—whether the most accurately predicted pathway corresponds to visible morphological distinctions—we visualized and quantified reference and predicted pathway enrichment alongside tumor and adjacent non-tumor micro regions.

In parallel, RidgeCV model was applied to assess linear relationships between image-derived features and individual pathway activities and tissue microregions. Together, these complementary approaches allowed us to evaluate how well biologically meaningful information in histology images may be represented by experimentally derived pathway enrichment at micro resolution.

Fig. 1 Study design and overview



a, Workflow of predicting pathway enrichment score and tumor and adjacent non-tumor micro areas. Visual features are extracted from H&E image spot using UNI2-h and used as input to RF or RidgeCV to make the predictions. **b**, Seven-step workflow, begin by extracting image spots and annotating them with spatial coordinates, followed by selecting, processing, and computing pathway enrichment scores from ST data. Patient metadata are then integrated with the spots and pathway enrichment data to support model development, enable train-test splitting, and prevent data leakage. **c**, Summary of datasets: Dataset I (He et al., 2020) includes 23 breast cancer patients across 5 subtypes; Dataset II (Andersson et al., 2021) contains 4 HER2-positive breast cancer patients; Dataset III (Zuani et al., 2024) includes 8 NSCLC tumors and 8 adjacent lung tissues across 16 sections per condition. *, # indicates seven-fold cross-validation; one fold is shown to illustrate training and internal testing composition. Data from the same patient were kept mutually exclusive in training and testing sets in Dataset I & III. Dataset II is used for external testing only. § denotes sections/slides from unique patients. STv1, an earlier version of ST generated following the protocols described by Ståhl et al.

Predicting pathway enrichment activity from paired histology-derived features at approximately 100µm resolution using RF and seven-fold patient-wise cross validation on Dataset I.

We developed a multi-stage computational workflow to predict pathway enrichment directly from H&E-stained histology images (Fig. 1b and Methods). Eleven pathways implicated in tumor biology and immune regulation were initially selected (Table 1), seven of which—Estrogen, VEGF, TGFβ, NF-κB, Wnt, MAPK, and PI3K-Akt—overlap with PROGENy-supported pathways. For each image spot, pathway PROGENy scores were computed as a weighted sum of the top 100 signature genes' log_{1p} counts per million (CPM), using default gene–pathway weights. Scores were normalized to a [-1, 1] range based on 1,000 random permutations of log_{1p} CPM values, where positive scores indicate higher-than-expected pathway

activity, and negative scores reflect lower-than-expected activity relative to the permuted reference.

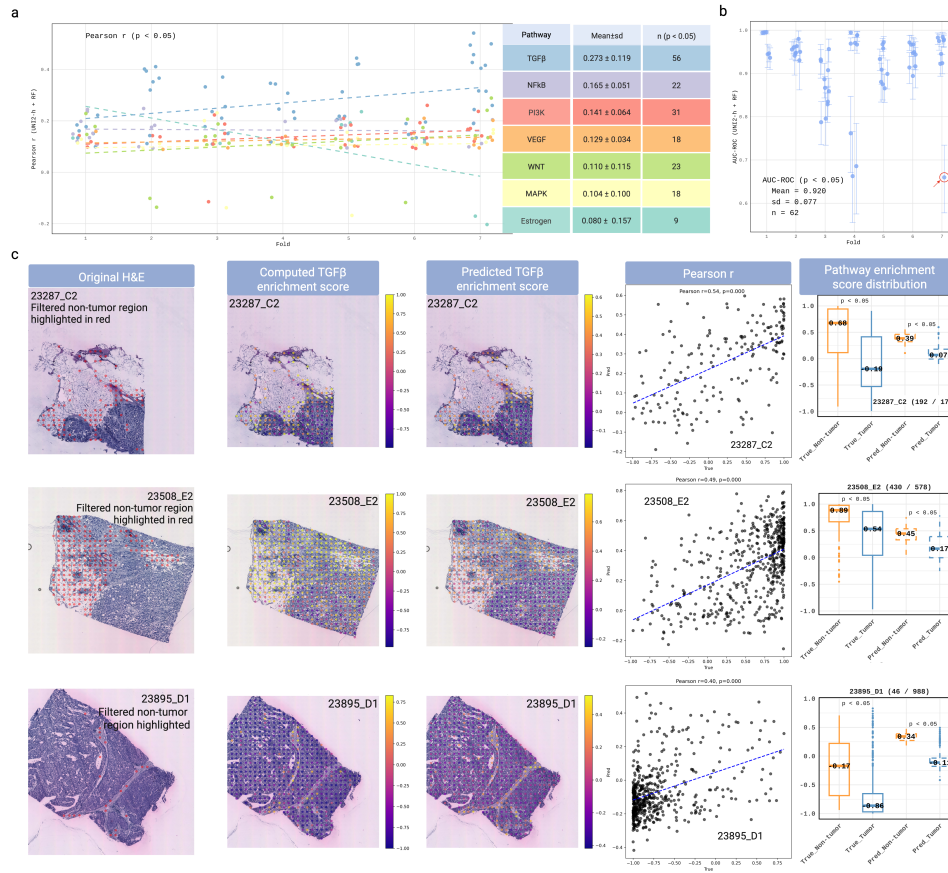
For the breast cancer ST dataset I (He et al., 2020^[18]), separate RF models were trained for each prediction task: seven individual pathways and tumor versus adjacent non-tumor micro-regions. Each model used 1,536-dimensional histology-derived features from image spots. Model performance was evaluated via patient-wise stratified seven-fold cross-validation. In addition, for each fold, the trained model was tested on the external Dataset II (Andersson et al., 2021^[19]) to assess fold-specific generalization. Pathway enrichment predictions were quantified using Pearson correlation coefficients, whereas tumor versus non-tumor classification was measured by Area Under the Receiver Operating Characteristic Curve (AUC-ROC).

Among the seven pathways analyzed, six exhibited positive Pearson's r values, with TGF β signaling achieving the highest predictive performance (Fig. 2a). Statistically significant correlations (two-tailed t test, $p < 0.05$) were observed in 56 of 68 tissue sections, with an average Pearson r of 0.273. NF- κ B followed, showing a significant correlation in 22 sections with an average r of 0.165. Tumor versus non-tumor prediction achieved an average AUC-ROC of 0.920 (one-tailed t test, $p < 0.05$) across folds. After excluding sections containing only tumor regions, 62 sections were retained for this analysis (Fig. 2b), indicating that histology-derived features effectively captured differences between tumor and adjacent non-tumor microregions.

Filtering for sections that showed statistically significant Pearson correlations and contained both tumor and non-tumor microregions yielded 52 sections for detailed analysis of TGF β signaling. Generally consistent trends in computed and predicted PROGENy scores, alongside spatial tumor annotations, were observed. (Fig. 2c). In section 23287_C2, for example, the Pearson r between computed and predicted TGF β activity was 0.54. In the same section, with 192 non-tumor and 176 adjacent tumor microregions, computed TGF β activity was higher in non-tumor microregions (median 0.68) than in adjacent tumor microregions (median -0.19 ; Mann-Whitney U test, $p < 0.05$). Predicted TGF β activity mirrored this trend (median 0.39 vs. 0.07; $p < 0.05$).

Across the 52 sections, 46 (88.5%) displayed similar trends: for both computed and predicted TGF β signaling, median activity levels were higher in non-tumor microregions than in adjacent tumor microregions. Of these 46 sections, 34 reached statistical significance in both measures, 11 were significant only for predicted activity, and 1 showed no significance in either. These trends are consistent with the established role of TGF β in modulating the tumor microenvironment, including, among other mechanisms, activating fibroblasts and remodeling the extracellular matrix^[20,21]. Six sections exhibited reversed trends, in which computed TGF β activity was higher in tumor microregions, whereas predicted activity was higher in non-tumor regions. Only one of these sections showed a statistically significant difference for computed activity, while all six were significant for predicted activity. These observations highlight that predicted TGF β activity generally captures local differences, whereas the computed measure is less sensitive to upregulated TGF β activity in tumor microregions. Overall, TGF β activity tends to be higher in tumor-adjacent non-tumor microregions, and this overall trend is generally captured by the predictive models, although some heterogeneity remains.

Figure 2. Predictive performance of the RF model on pathway enrichment and tumor annotation on breast cancer Dataset I.



a. Performance of the RF models in predicting pathway enrichment across seven pathways in Dataset I using seven-fold patient-wise cross-validation, quantified by Pearson’s correlation coefficient (r). Each dot represents a tissue section; statistically significant Pearson correlations (two-tailed t test, $p < 0.05$) are indicated. Mean \pm sd stands for the mean value plus or minus the standard deviation. n represents the number of sections with $p < 0.05$. **b.** Tumor versus adjacent non-tumor prediction performance, measured by AUC-ROC (one-tailed t test, $p < 0.05$) across tissue sections. Each point represents a section, with vertical lines indicating the 95% confidence interval. The section with lower AUC-ROC, highlighted by a red circle and arrow, corresponds to a mislabeled section (Section D1, patient 23287), where multiple non-tumor spots were incorrectly annotated as tumor. Some annotation issue is shown in the yellow-boxed region of Supplementary Fig. 1. **c.** Example visualization of computed versus predicted TGF β pathway activity in representative tissue sections (testing sections on fold seven). From left to right: (i) original H&E section with filtered non-tumor microregions highlighted in red at the spot level; (ii) computed TGF β pathway activity overlaid on the H&E image, with the color bar representing the range of activity values; (iii) predicted TGF β pathway activity mapped onto the H&E image, with the color bar representing the range of activity values; (iv) scatter plot showing Pearson correlation between computed (x-axis, labeled “true”) and predicted (y-axis, labeled “pred”) TGF β activity, with associated p -value; (v) distribution of pathway enrichment activity across tumor and non-tumor microregions, with Mann–Whitney U test p -values for computed and predicted TGF β activity, respectively. The ratio of non-tumor to tumor microregion counts is also indicated as (non-tumor counts / tumor counts). The central line within each box represents the median activity value, with the overlaid numbers denoting the corresponding medians.

External validation of pathway enrichment prediction in Dataset II

To assess the generalizability of the models trained on Dataset I, we applied them to an independent breast cancer ST dataset (Dataset II, Fig. 1c) as an external test following each fold

of the seven-fold cross-validation. Four sections from four different patients in Dataset II were included for the external testing. Histology feature extraction and reference pathway activities were generated and computed using the same methods as for Dataset I. Performance was evaluated using the same metrics as in Dataset I as well.

Among the pathways, same six exhibited positive Pearson's r values, with TGF β signaling on top. Statistically significant correlations (two-tailed t test, $p < 0.05$) were observed in all four tissue sections. For seven repeats, this amounted to 28 significant correlations in total, with an average r of 0.267. NF κ B followed closely, with an average r of 0.274, showing significance in nearly all tissue sections (27 significant correlations across seven repeats) (Supplementary Fig. 2a). WNT also achieved a comparable r of 0.274; however, only one of the four tissue sections showed statistically significant correlation, totaling seven across the seven folds, indicating higher variability across patient data. Tumor versus non-tumor prediction achieved an average AUC-ROC of 0.884 (one-tailed t test, $p < 0.05$) (Supplementary Fig. 2b).

Visualization of the external test results revealed that computed and predicted PROGENy scores, alongside spatial tumor annotations, exhibited similar patterns (Supplementary Fig. 2c). For example, in section A1, the Pearson correlation between computed and predicted TGF β activity was 0.31. In this section, with 78 non-tumor and 600 adjacent tumor microregions, computed TGF β activity was higher in non-tumor microregions (median 0.63) than in adjacent tumor microregions (median 0.37; Mann–Whitney U test, $p < 0.05$), and predicted TGF β activity mirrored this trend (median 0.36 vs. 0.19; Mann–Whitney U test, $p < 0.05$). Two of the four sections displayed similar non-tumor versus tumor trends between computed and predicted TGF β activity, with statistical significance in both. One section showed no significance in either, and the remaining section was significant only in predicted activity. These patterns were consistent across all seven folds of the external test. Overall, the external validation confirmed that the model could reliably capture the spatial differences in TGF β activity, in line with the trends previously observed in Dataset I.

Generalization to NSCLC at higher spatial resolution

To test generalizability across cancer types, we retrained the workflow on an human non-small cell lung cancer (NSCLC) ST dataset (Dataset III^[22] and Fig. 1c). Dataset III contains separate sections for tumor and adjacent non-tumor regions. We first paired each tumor section with a corresponding non-tumor section from the same patient based on patient names, resulting in 16 pairs, ensuring that each pair included both tumor and non-tumor micro regions. Histology feature extraction and reference pathway activity computation were performed using the same methods as for Datasets I and II. Performance was evaluated using the same metrics as well.

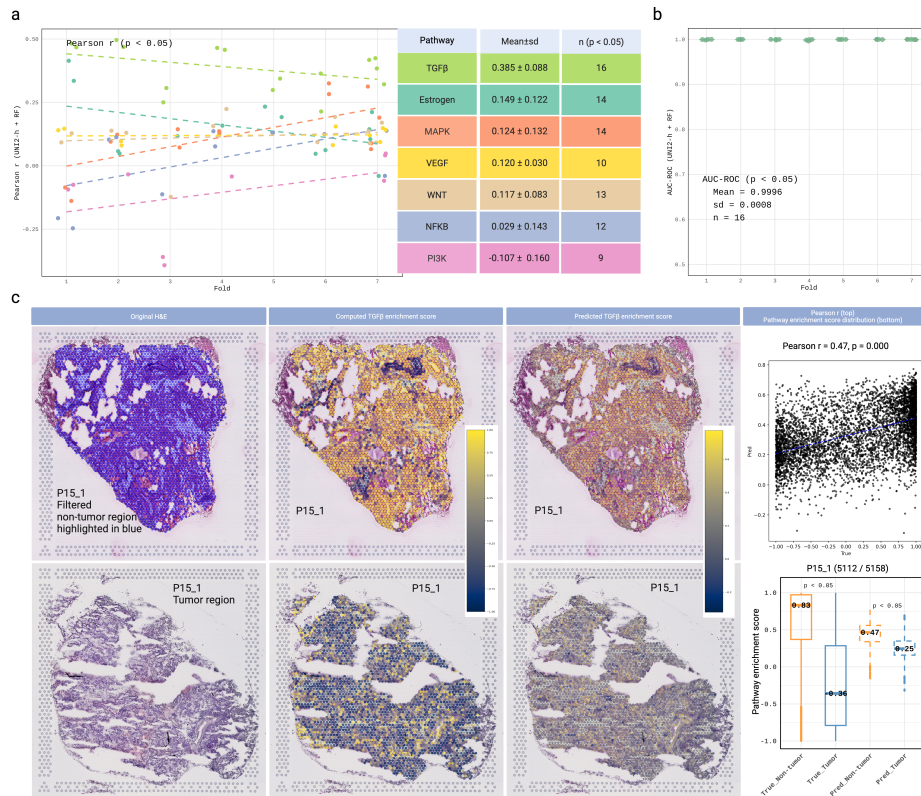
Predicted pathway activity in NSCLC closely mirrored the breast cancer results for the TGF β signaling, which was consistently the most accurately predicted pathway. Statistically significant Pearson correlations (two-tailed t test, $p < 0.05$) were observed in 16 of 16 paired issue sections, with an average Pearson r of 0.385 (Fig. 4a). Tumor versus non-tumor prediction reached an average AUC-ROC of 1 (one-tailed t test, $p < 0.05$) across all folds.

Visualizing computed and predicted PROGENy scores alongside spatial tumor annotations revealed similar patterns, six exhibited positive Pearson's r values, with TGF β signaling

achieving the highest predictive performance (Fig. 4a). For example, in paired section P15_1, the Pearson correlation between computed and predicted TGF β activity was 0.47. In the same pair, with 5,112 non-tumor and 5,158 adjacent tumor microregions, computed TGF β activity was higher in non-tumor microregions (median 0.83) than in adjacent tumor microregions (median – 0.36; Mann–Whitney U test, $p < 0.05$). Predicted TGF β activity mirrored this trend (median 0.47 vs. 0.25; $p < 0.05$). Across the 16 paired sections, 14 (87.5%) displayed similar non-tumor versus tumor trends between computed and predicted TGF β activity, all reaching statistical significance.

Two paired sections (12.5%) exhibited reversed trends, in which computed TGF β activity was higher in tumor microregions, whereas predicted activity was higher in non-tumor regions. These sections also showed statistically significant differences for both computed and predicted TGF β activity. These observations highlight that, similar to what was observed in breast cancer, predicted TGF β activity generally captures local differences, while the model is less effective at detecting upregulated TGF β activity in tumor microregions.

Figure 3. Predictive performance of the RF model on pathway enrichment and tumor annotation on NSCLC dataset III.



a. Performance of the RF models in predicting pathway enrichment across seven pathways in Dataset III using seven-fold patient-wise cross-validation, quantified by Pearson’s correlation coefficient (r). Each dot represents a tissue section; statistically significant Pearson correlations (two-tailed t test, $p < 0.05$) are indicated. Mean \pm sd stands for the mean value plus or minus the standard deviation. n represents the number of sections with $p < 0.05$. **b.** Tumor versus adjacent non-tumor prediction performance, measured by AUC-ROC (one-tailed t test, $p < 0.05$) across tissue sections. Each point represents a section, with vertical lines indicating the 95% confidence interval. **c.** Example visualization of computed versus predicted TGF β pathway activity in representative tissue sections (testing sections on fold 1 for dataset III). From left to right: (i) original H&E section with filtered non-tumor microregions

highlighted in blue at the spot level; (ii) computed TGF β pathway activity overlaid on the H&E image, with the color bar representing the range of activity values; (iii) predicted TGF β pathway activity mapped onto the H&E image, with the color bar representing the range of activity values; (iv top) scatter plot showing Pearson correlation between computed (x-axis, labeled “true”) and predicted (y-axis, labeled “pred”) TGF β activity, with associated p-value; (iv bottom) distribution of pathway enrichment activity across tumor and non-tumor microregions, with Mann–Whitney U test p-values for computed and predicted TGF β activity, respectively. The ratio of non-tumor to tumor microregion counts is also indicated as (non-tumor counts / tumor counts). The central line within each box represents the median activity value, with the overlaid numbers denoting the corresponding medians.

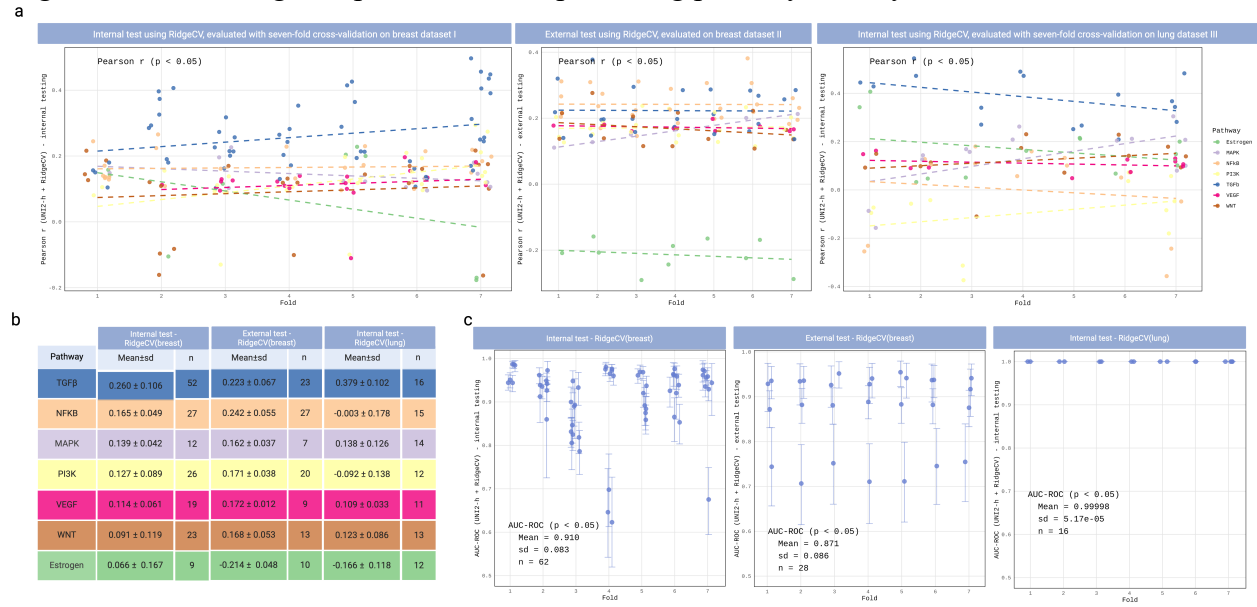
Assessing linear RidgeCV performance across ST datasets

To evaluate linear relationships between image-derived features and individual pathway activities, we substituted the RF with linear RidgeCV to predict pathway activity from UNI2-h–extracted histology features, keeping all other steps unchanged. Results are displayed in Fig. 4 and Supplementary Fig. 3.

Linear RidgeCV produced results comparable to RF predictions. As shown in Figs. 4a and 4b, TGF β pathway activity consistently exhibited the top prediction performance across all three datasets. Spatial mapping of TGF β activity revealed similar trends as well (Supplementary Figs. 3 and 4). In dataset I, 43 of the 49 sections (87.8%) showed consistent non-tumor versus tumor trends between computed and predicted TGF β activity, with higher activity in non-tumor microregions compared with adjacent tumor microregions. Of these, 28 sections were statistically significant in both, 12 were significant only in predicted activity, 2 were significant only in computed activity, and 1 showed no significant difference in either. Six sections exhibited reversed trends. In these, computed TGF β activity was higher in tumor microregions (2 statistically significant, 4 non-significant), whereas predicted activity was higher in non-tumor regions in 2 sections (both statistically significant) and lower in the remaining 4 sections (non-significant). Of these, the sections with significant computed activity do not coincide with those with significant predicted activity.

Comparable results were observed in datasets II and III as well. In dataset II, two of the four sections displayed consistent trends, higher activity in non-tumor microregions compared with adjacent tumor microregions, with statistical significance in both computed and predicted activity. One section showed no significance in either, and one section was significant only in predicted activity. For dataset III, across 16 paired sections, 14 (87.5%) showed consistent trends, higher activity in non-tumor microregions compared with adjacent tumor microregions, between computed and predicted TGF β activity, all of which were statistically significant. Two paired sections (12.5%) exhibited reversed trends, with computed activity higher in tumor microregions and predicted activity higher in non-tumor microregions, both reaching statistical significance.

Figure 4. Linear RidgeCV performance in predicting pathway activity across three ST datasets.



a. RidgeCV model performance in predicting enrichment for seven pathways in Datasets I (seven-fold patient-wise cross-validation), II (external testing using models trained on Dataset I for each fold), and III (seven-fold patient-wise cross-validation) (left to right), quantified by Pearson’s correlation coefficient (r). Each dot represents a tissue section; statistically significant correlations (two-tailed t test, $p < 0.05$) are indicated. **b.** Mean \pm sd represents the mean \pm standard deviation across the three datasets. **c.** Tumor versus adjacent non-tumor prediction performance, measured by AUC-ROC (one-tailed t test, $p < 0.05$) across tissue sections for the three datasets. Each point represents a section, with vertical lines showing the 95% confidence interval.

Discussion

In this study, we present a computational framework that leverages histology-derived features to predict spatial pathway enrichment at approximately 55-100 microscale resolution using both linear and non-linear models. By systematically evaluating our approach across three independent datasets spanning breast and lung cancers, we demonstrate that morphology-informed predictions could capture biologically meaningful and spatially coherent pathway enrichment pattern. Notably, five out of seven pathways—VEGF, TGF β , NF- κ B, Wnt, and MAPK—demonstrated consistently positive Pearson correlations between predicted and experimentally derived pathway enrichment across all datasets.

Moreover, to better understand and interpret how pathway enrichment is reflected in histology, we examined both model behavior and pathway-specific performance. First, the comparable accuracy achieved by linear and non-linear models indicates that the morphological correlates of pathway activity are largely captured within linearly accessible feature space. Second, the pathway with the highest predictive accuracy, TGF β (mean Pearson $r = 0.267$ – 0.385), aligns with well-established morphological distinctions between tumor and adjacent non-tumor microregions, providing a biological basis for its stronger image-derived signal. Third, predictions of tumor versus adjacent non-tumor regions further confirmed that these morphological contrasts were effectively retained in the extracted visual features (mean AUC-ROC = 0.884 – 1.00).

Compared with 10 previously published frameworks that leverage histology images to predict spatial gene expression, none directly predicted pathway enrichment, and only four reported downstream analyses at the pathway level. [7,23,24,25,26,27,28,29,30,31] In those four studies, pathway analyses were typically indirect. Genes were first selected based on high variability, elevated expression, or other criteria, predicted from histology images, and subsequently associated with known pathways. For instance, Hist2ST linked certain predicted genes—selected based on their top enriched pathway—to the human papillomavirus infection pathway in breast cancer ST datasets, without spatially resolved or quantitative insights into pathway relevance.^[26] Although the HPV infection pathway has been reported in association with breast cancer, it is likely of limited biological relevance compared with canonical breast cancer pathways such as Estrogen signaling, MAPK, or TGF β . This indirect strategy contrasts with our framework, which enables direct, spatially resolved, pathway-level inference from histology images.

Despite these advances, several limitations warrant consideration. First, while our framework robustly predicts TGF β pathway activity in 87–88% of sections showing higher expression in non-tumor microregions compared with adjacent tumor microregions, its sensitivity is low in sections with reversed expression patterns. This may be because the model primarily infers TGF β activity based on contrasts between tumor and adjacent non-tumor microregions; when tumor regions with high TGF β activity constitute a smaller fraction of the datasets, the model has less information to detect these signals, resulting in reduced sensitivity. Second, the ST datasets used in our study are of moderate size, and the use of larger, more diverse, and representative datasets could further enhance the predictive performance of our framework. Third, our study is constrained to ST data, integrating additional multi-omics layers (e.g., single-cell transcriptomics and proteomics) could improve prediction resolution, accuracy, and biological interpretability. Finally, extending our approach to downstream applications, such as treatment response prediction, may further strengthen its translational relevance.

Methods

Datasets

We obtained three ST datasets separately from He et al. (Dataset I; breast cancer), Andersson et al. (Dataset II; breast cancer), and Zuani et al. (Dataset III; lung cancer). Datasets I and II were generated following the protocols described by Ståhl et al., with a section thickness of 16 μm , a spot diameter of 100 μm , and a center-to-center distance of 200 μm . Dataset III was generated using the 10 \times Genomics Visium platform with a section thickness of 10 μm , a spot diameter of 55 μm , and a center-to-center distance of 100 μm . Further sample and section information are detailed in Fig. 1c and corresponding reference articles.

ST data processing and pathway enrichment computation

For the ST data, spots with a total expression count below 1000 or fewer than 200 detected genes were excluded. The gene expression counts measured from the remaining spots were then normalized by dividing each gene's expression by the total counts for that spot, multiplying by 1,000,000 (counts per million), and applying a natural logarithmic transformation ($\log_1 p$).

Using the selected pathways detailed in Table 1—seven of which (Estrogen, VEGF, TGF β , NF- κ B, Wnt, MAPK, and PI3K-Akt) overlap with PROGENy-supported pathways—the top 100 PROGENy signature genes for each pathway were selected. Replicated genes were removed, and

the remaining unique genes, along with their processed expression values for each spot, were extracted. Spot-level pathway activity scores were then computed using the progenyPerm function. Specifically, a PROGENy weight matrix for human pathways was obtained via getModel("Human", top = 100), and the corresponding gene expression data for the seven pathways were supplied to progenyPerm with 1,000 permutations, keeping absolute scores (z_scores = FALSE). This procedure produces reference pathway activity scores at the spot level for downstream prediction tasks.

Histology image was divided into N patches, where N corresponds to the number of spots retained after filtering, ensuring a one-to-one correspondence between image patches and pathway expression profiles. Each patch consisted of three color channels and had dimensions of $W \times H$ pixels. To approximately match the diameter of the spots, W and H were set to 112 pixels for datasets I, II, and III. The spot-level pathway activity and morphology were linked by the spatial coordinates, sample, and section names.

Table 1. Selected pathways for this study.

Pathways	Description & source
ErbB signaling pathway	https://www.kegg.jp/entry/map04012
PI3K-Akt signaling pathway	https://www.kegg.jp/entry/map04151
MAPK signaling pathway	https://www.kegg.jp/entry/map04010
Estrogen signaling pathway	https://www.kegg.jp/entry/map04915
mTOR signaling pathway	https://www.kegg.jp/entry/map04150
Wnt signaling pathway	https://www.kegg.jp/entry/map04310
Cell cycle	https://www.kegg.jp/entry/map04110
NF-kappa B signaling pathway	https://www.kegg.jp/entry/map04064
TGF-beta signaling pathway	https://www.kegg.jp/entry/map04350
VEGF signaling pathway	https://www.kegg.jp/entry/map04370
PD-L1 expression and PD-1 checkpoint pathway in cancer	https://www.kegg.jp/entry/map05235

Framework overview

We developed a computational framework that directly predicts pathway activity, and tumor and adjacent non-tumor micro regions from histopathological image patches by combining deep feature extraction from a computational pathology foundation with RF or RidgeCV models. Input data consisted of spatially resolved histopathological image spots and a corresponding CSV file containing patient metadata and pathway activity. Mathematically, the overall process can be summarized as:

$$\hat{y}_p = f_p (F_{UNI2-h}(T(Ip)))$$

Where I_p represents the input histology image for spot p , $T(\cdot)$ denotes preprocessing and color normalization, $F_{UNI2-h}(\cdot)$ is the UNI2-h feature extractor, $f_p(\cdot)$ is the model selected to predict pathway activity or tumor non-tumor microregion, and \hat{y}_p represents the prediction outcome.

Model Training, cross-validation, and external validation

A seven-fold patient-wise cross-validation strategy was employed to train and test model performance, using patients as the grouping variable to ensure that images from the same patient did not appear in both training and test sets. Detailed train-test size distribution is shown in Fig. 1c. Color normalization was performed, the normalization parameters (mean and standard deviation) were computed from a random subset (10%) of training images within each fold. These normalization statistics were then applied to all corresponding training, testing images and external testing images if applicable.

Within the training set, the pretrained UNI2-h model was used to extract 1,536 visual features from each histology spot. Pathway activities or tumor versus non-tumor microregions were then predicted from these features using either RF or RidgeCV models. Model performance was evaluated using the Pearson correlation coefficient between predicted and measured pathway enrichment scores and the AUC-ROC for tumor versus non-tumor microregion prediction. For internal testing within each fold, the trained models were applied to predict pathway activities or tumor versus non-tumor microregions from the 1,536 visual features extracted from the test set. The same procedure was applied to external test datasets when available.

Implementation details and reproducibility

All experiments were implemented in Python using PyTorch for feature extraction and scikit-learn for regression, classification, and preprocessing. Random seeds were fixed for NumPy and PyTorch to ensure reproducibility. Images were processed in batches using DataLoader objects, with appropriate shuffling applied during training. Computations were performed on GPU-enabled hardware. Hyperparameters such as RF settings (200 trees, no maximum depth specified) were selected. RidgeCV with L2 regularization was applied, with the regularization strength (α) spanning 10^{-3} to 10^8 , to be automatically determined for each pathway and tumor non-tumor microregion prediction. After fitting, the model with the optimal alpha was used to predict both the internal test set and external test set (when available).

Model evaluation

To quantify predictive performance, we computed the Pearson correlation coefficient between predicted and measured pathway enrichments:

$$r_{p,i} = \frac{\text{cov}(\hat{y}_{p,i}, y_{p,i})}{\sigma_{\hat{y}_{p,i}} \sigma_{y_{p,i}}}$$

Where $\hat{y}_{p,i}$ and $y_{p,i}$ are the predicted and true enrichment values for pathway i at spot p for a given section, respectively, with i ranging from one to seven. The corresponding two-tailed p-value was calculated from t-distribution with the null hypothesis that $r=0$ and no linear correlation between predicted and measured enrichment values in a given section. For tumor and non-tumor microregion prediction, performance was evaluated using AUC-ROC, 95% CI, and one tailed p-value. The null hypothesis tested was that the prediction performed no better than random chance ($AUC-ROC = 0.5$).

In datasets I and III, performances were calculated for each fold on the held-out internal test set, providing fold-wise estimates of model generalization. For dataset II, they were calculated for each section. Summary statistics including mean and standard deviation across pathways per were reported to for assessment.

Other statistical analysis

Bootstrap resampling was applied with 1,000 iterations for each pathway to estimate 95% CI.

Computational setup

Data processing, model development, and heavy computing were conducted on a Python 3 environment running on Google Compute Engine (the server was equipped with 12.7 GB of system RAM and 108 GB of disk storage) and on four NVIDIA A100-SXM4-80GB GPUs.

Data availability

The data used in this study are available at:

Mendeley (<https://data.mendeley.com/datasets/29ntw7sh4r/5>),

Zenodo (<https://zenodo.org/records/3957257#.Y4LB-rLMIfg>),

and ArrayExpress (E-MTAB-13530, <https://www.ebi.ac.uk/biostudies/arrayexpress/studies/E-MTAB-13530>), with appropriate references. We also requested the original H&E sections for our lung cancer dataset; these are not publicly available, and we are not permitted to upload or share them.

Code availability

The code used to develop the framework and generate results in this study is available in GitHub at <https://github.com/lingliao/ISTME>.

Author Contributions

L.L. : Conceptualization, data collection, investigation, methodology, formal analysis, software, visualization, and draft and review manuscript.

C.Y. : Conceptualization, model structure, statistical analysis, and reviewed the manuscript.

Maxim Artyomov: Provided critical input on study conceptualization, model structure, and reviewed the manuscript.

A.K. : Provided critical input on study conceptualization, model structure, genetic data processing, and reviewed the manuscript.

M.W. : Provided critical input on study conceptualization, biological interpretation, and reviewed the manuscript.

H.Z. : Provided critical input on methodology and software.

Alexey Sergushichev: Provided critical input on methodology, visualization, pathway enrichment tool selection, and reviewed the manuscript.

R.C. : Conceptualization, provided critical input on data curation and processing, visualization, review and edited the manuscript, and supervised the overall work.

Acknowledgements

We thank Kilannin Krysiak, Anthony Williams, Somnath Paul, Dian Li, and Siyu (Steven) Lin for their valuable suggestions and input on experimental design, data processing, and other aspects of this study. We are also grateful to Ana Cvejic for generously providing the original whole-slide images used in this work. Finally, L.L. gratefully acknowledges the consistent support from the McDonnell Scholars Academy at Washington University in St. Louis.

Conflict of Interests

L.L is the founder of Biomedical Deep Learning LLC. C.Y., M.A., M.W., A.K., H.Z., and R.C. declare no competing interests.

Reference

- [1] Ståhl, P. L. et al. Visualization and analysis of gene expression in tissue sections by spatial transcriptomics. *Science* 353, 78–82 (2016).
- [2] Marx, V. Method of the Year: spatially resolved transcriptomics. *Nat Methods* 18, 9–14 (2021). <https://doi.org/10.1038/s41592-020-01033-y>
- [3] Williams, C.G., Lee, H.J., Asatsuma, T. et al. An introduction to spatial transcriptomics for biomedical research. *Genome Med* 14, 68 (2022). <https://doi.org/10.1186/s13073-022-01075-1>
- [4] Emory National Primate Research Center. (2025, April 30). EPC Genomics Core rates. Emory University. Retrieved October 23, 2025, from https://enprc.emory.edu/nhp_genomics_core/rates/index.html
- [5] University of Pittsburgh Center for Advanced Genomics. (2025, October 1). Pricing. Retrieved October 23, 2025, from <https://www.advancedgenomics.pitt.edu/pricing>
- [6] University of Wisconsin–Madison Gene Expression Center. (2025, September). NanoString GeoMx Spatial Transcriptomics pricing. Retrieved October 23, 2025, from <https://biotech.wisc.edu/gec/spatial-transcriptomics-services/nanostring-geomx-spatial-transcriptomics/#pricing>
- [7] Wang, C., Chan, A.S., Fu, X. et al. Benchmarking the translational potential of spatial gene expression prediction from histology. *Nat Commun* 16, 1544 (2025). <https://doi.org/10.1038/s41467-025-56618-y>
- [8] Raj A, van Oudenaarden A. Nature, nurture, or chance: stochastic gene expression and its consequences. *Cell*. 2008 Oct 17;135(2):216-26. doi: 10.1016/j.cell.2008.09.050. PMID: 18957198; PMCID: PMC3118044.
- [9] Raj A, van Oudenaarden A. Nature, nurture, or chance: stochastic gene expression and its consequences. *Cell*. 2008 Oct 17;135(2):216-26. doi: 10.1016/j.cell.2008.09.050. PMID: 18957198; PMCID: PMC3118044.
- [10] Weidemann DE, Holehouse J, Singh A, Grima R, Hauf S. The minimal intrinsic stochasticity of constitutively expressed eukaryotic genes is sub-Poissonian. *Sci Adv*. 2023 Aug 9;9(32):eadh5138. doi: 10.1126/sciadv.adh5138. Epub 2023 Aug 9. PMID: 37556551; PMCID: PMC10411910.
- [11] Wackerly DD, Mendenhall III W, Scheaffer RL. Multivariate probability distributions. In: *Mathematical Statistics with Applications*. 2008:7th ed. Belmont, CA: Brooks/Cole; 223–295.
- [12] Massagué J. TGFbeta in Cancer. *Cell*. 2008 Jul 25;134(2):215-30. doi: 10.1016/j.cell.2008.07.001. PMID: 18662538; PMCID: PMC3512574.
- [13] Pickup M, Novitskiy S, Moses HL. The roles of TGFβ in the tumour microenvironment. *Nat Rev Cancer*. 2013 Nov;13(11):788-99. doi: 10.1038/nrc3603. Epub 2013 Oct 17. PMID: 24132110; PMCID: PMC4025940.
- [14] Battle E, Massagué J. Transforming Growth Factor-β Signaling in Immunity and Cancer. *Immunity*. 2019 Apr 16;50(4):924-940. doi: 10.1016/j.immuni.2019.03.024. PMID: 30995507; PMCID: PMC7507121.
- [15] Chan MK, Chung JY, Tang PC, Chan AS, Ho JY, Lin TP, Chen J, Leung KT, To KF, Lan HY, Tang PM. TGF-β signaling networks in the tumor microenvironment. *Cancer Lett*. 2022 Dec 1;550:215925. doi: 10.1016/j.canlet.2022.215925. Epub 2022 Sep 29. PMID: 36183857.

- [16] Chen, R. J., Ding, T., Lu, M. Y., Williamson, D. F. K., Jaume, G., Chen, B., Zhang, A., Shao, D., Song, A. H., Shaban, M., & others. (2024). Towards a general-purpose foundation model for computational pathology. *Nature Medicine*.
- [17] Schubert, M., Klinger, B., Klünemann, M. et al. Perturbation-response genes reveal signaling footprints in cancer gene expression. *Nat Commun* 9, 20 (2018). <https://doi.org/10.1038/s41467-017-02391-6>
- [18] He, B., Bergenstråhle, L., Stenbeck, L. et al. Integrating spatial gene expression and breast tumour morphology via deep learning. *Nat Biomed Eng* 4, 827–834 (2020). <https://doi.org/10.1038/s41551-020-0578-x>
- [19] Andersson, A., Larsson, L., Stenbeck, L. et al. Spatial deconvolution of HER2-positive breast cancer delineates tumor-associated cell type interactions. *Nat Commun* 12, 6012 (2021). <https://doi.org/10.1038/s41467-021-26271-2>
- [20] Shi, X., Yang, J., Deng, S. et al. TGF- β signaling in the tumor metabolic microenvironment and targeted therapies. *J Hematol Oncol* 15, 135 (2022). <https://doi.org/10.1186/s13045-022-01349-6>
- [21] Zhao, Y., Shen, M., Wu, L. et al. Stromal cells in the tumor microenvironment: accomplices of tumor progression?. *Cell Death Dis* 14, 587 (2023). <https://doi.org/10.1038/s41419-023-06110-6>
- [22] De Zuani, M., Xue, H., Park, J.S. et al. Single-cell and spatial transcriptomics analysis of non-small cell lung cancer. *Nat Commun* 15, 4388 (2024). <https://doi.org/10.1038/s41467-024-48700-8>
- [23] Zhang, D., Schroeder, A., Yan, H. et al. Inferring super-resolution tissue architecture by integrating spatial transcriptomics with histology. *Nat Biotechnol* 42, 1372–1377 (2024). <https://doi.org/10.1038/s41587-023-02019-9>
- [24] Monjo, T., Koido, M., Nagasawa, S. et al. Efficient prediction of a spatial transcriptomics profile better characterizes breast cancer tissue sections without costly experimentation. *Sci Rep* 12, 4133 (2022). <https://doi.org/10.1038/s41598-022-07685-4>
- [25] Hoang, D.T., Dinstag, G., Shulman, E.D. et al. A deep-learning framework to predict cancer treatment response from histopathology images through imputed transcriptomics. *Nat Cancer* 5, 1305–1317 (2024). <https://doi.org/10.1038/s43018-024-00793-2>
- [26] Yuansong Zeng, Zhuoyi Wei, Weijiang Yu, Rui Yin, Yuchen Yuan, Bingling Li, Zhonghui Tang, Yutong Lu, Yuedong Yang, Spatial transcriptomics prediction from histology jointly through Transformer and graph neural networks, *Briefings in Bioinformatics*, Volume 23, Issue 5, September 2022, bbac297, <https://doi.org/10.1093/bib/bbac297>
- [27] Chongyue Zhao, Zhongli Xu, Xinjun Wang, Shiyue Tao, William A MacDonald, Kun He, Amanda C Poholek, Kong Chen, Heng Huang, Wei Chen, Innovative super-resolution in spatial transcriptomics: a transformer model exploiting histology images and spatial gene expression, *Briefings in Bioinformatics*, Volume 25, Issue 2, March 2024, bbae052, <https://doi.org/10.1093/bib/bbae052>
- [28] Fu, X., Cao, Y., Bian, B. et al. Spatial gene expression at single-cell resolution from histology using deep learning with GHIST. *Nat Methods* 22, 1900–1910 (2025). <https://doi.org/10.1038/s41592-025-02795-z>
- [29] Yuran Jia, Junliang Liu, Li Chen, Tianyi Zhao, Yadong Wang, THItGene: a deep learning method for predicting spatial transcriptomics from histological images, *Briefings in Bioinformatics*, Volume 25, Issue 1, January 2024, bbad464, <https://doi.org/10.1093/bib/bbad464>

- [30] Yang, Y., Hossain, M. Z., Stone, E. A. & Rahman, S. Exemplar guided deep neural network for spatial transcriptomics analysis of gene expression prediction. In Proc. 2023 IEEE/CVF Winter Conference on Applications of Computer Vision (WACV) 5039–5048 (IEEE, 2023).
- [31] Yang, Y., Hossain, M. Z., Stone, E. & Rahman, S. Spatial transcriptomics analysis of gene expression prediction using exemplar guided graph neural network. *Pattern Recognit.* 145, 109966 (2024).